energies

MDPI

Article

Heat and Mass Transfer of Micropolar-Casson Nanofluid over Vertical Variable Stretching Riga Sheet

Nadeem Abbas [1] and Wasfi Shatanawi [1,2,3,*]

[1] Department of Mathematics and Sciences, College of Humanities and Sciences, Prince Sultan University, Riyadh 11586, Saudi Arabia; nabbas@psu.edu.sa
[2] Department of Medical Research, China Medical University Hospital, China Medical University, Taichung 40402, Taiwan
[3] Department of Mathematics, Faculty of Science, The Hashemite University, P.O. Box 330127, Zarqa 13133, Jordan
* Correspondence: wshatanawi@psu.edu.sa

Abstract: In this analysis, we considered a comparative study of micropolar Casson nanofluid flow on a vertical nonlinear Riga stretching sheet. Effects of thermal and velocity slip are considered under thermophoresis and Brownian motions. Select nonlinear PDEs transformed into nonlinear coupled ODEs using the set of suitable transformations. The nonlinear coupled ODEs are solved through a numerical technique along with the Runge–Kutta 4th-order scheme. The impacts of pertinent flow parameters on skin friction, Nusselt number, temperature, and velocity distributions are depicted through tabular and graphical form. Brownian motion and the magnitude of the Sherwood number have opposite performances; likewise, the Nusselt number and Brownian motion also have opposite performances. The Sherwood number and Nusselt number succeeded with higher values. The increment of the Casson fluid parameter declined with fluid velocity, which shows that thickness is reduced due to the increment of the Casson fluid parameter. Fluid velocity distribution curves show increasing behavior due to increments of the micropolar parameter.

Keywords: vertical Riga sheet; micropolar-Casson fluid; thermal slip; numerical technique

Citation: Abbas, N.; Shatanawi, W. Heat and Mass Transfer of Micropolar-Casson Nanofluid over Vertical Variable Stretching Riga Sheet. *Energies* **2022**, *15*, 4945. https://doi.org/10.3390/en15144945

Academic Editor: Artur Blaszczuk

Received: 11 June 2022
Accepted: 29 June 2022
Published: 6 July 2022

1. Introduction

Non-Newtonian fluids play an important role in the field of engineering and its related industries. Research on non-Newtonian liquids is prominent due to the wide range of potential uses, including the extraction of crude oil from petroleum products, the creation of plastic materials, and the development of syrup medications. Casson fluid is a non-Newtonian fluid with unique characteristics; it acts like an elastic solid and the basic equation includes a yield shear stress in this type of fluid. Non-Newtonian transport phenomena occur in a variety of mechanical and chemical engineering disciplines, as well as in food preparation. The authors of this study focused on investigating the mix of models of Casson and micropolar fluids in order to establish the theoretical results in different assumptions. We developed the mixed stress tensor of Casson fluid and micropolar fluid, which becomes the Casson micropolar fluid model. In our research, the Casson micropolar fluid, Brownian motion, and thermophoresis effects on the variable Riga stretching sheet is considered. Erigen [1] pioneered the micropolar fluid theory and highlighted the idea of thermo-micropolar fluid [2]. The micropolar fluid theory is familiar as an analytical miniature that can be used to characterize the action of non-Newtonian liquid in numerous constructive appliances. Micropolar fluids attract consideration from prosecutors, which has resulted in the spread of their application in industrial, accomplishment, and engineering uses. Micropolar fluid displays a conflict in the passage of fluid in relation to Newtonian fluid, which adds a large quantity of micropolar specification accompanying the absolute viscosity in the fluid flow. The micropolar fluid can be an intensely affective fluid medium

in the environmental aspect of the examination of laminar flow. Micropolar theory investigates the impact of micro-rotation in fluid mechanics that consist of micro-constituents that force rotation. Comprehensive analysis of the theory and its appliances is established in an article by Ariman et al. [3], as well as a recent book written by Lukaszewicz [4] and Eringen [5] on the application of microfluid. Ahmadi [6] discussed the boundary layer flow for micropolar fluid over a semi-infinite plate under the effects of natural, forced, or mixed convection. Jena and Mathur [7] introduced the similarity solutions for the incompressible thermo-micropolar fluid flow past vertical non-isothermal flat plates and highlighted the impacts of forced, natural, and mixed convection for thermo-micropolar fluid. Gorla et al. [8] expand on this work by developing the results of micropolar fluid asymptotic boundary layer flow. Bhargava et al. [9] highlighted the influence of micropolar fluid flow with mixed convection using the finite element scheme on porous surfaces. The time-dependent flow of micropolar fluid on a sheet was studied by Hayat et al. [10] using the HAM technique. Ahmad et al. [11] investigated the impact of viscous dissipation on micropolar fluid flow with a nonlinear stretching sheet. Reddy et al. [12] studied the time-dependent flow of micropolar fluid using a vertical slender hollow cylinder. Lund et al. [13] studied the MHD micropolar fluid flow over a vertical shrinking sheet. Dawar et al. [14] discussed the influence of chemical radiations and microstructural slip over a stretching sheet. Singh et al. [15] discussed the influence of micropolar fluid flow numerically. Several investigators are developing the results concerning dynamic problems (see Refs. [15–18]).

The past research on flow and heat transmission on stretching sheets caught the attention of scholars in a variety of fields. It is important in polyamide production due to the many mechanical developments of polymers. This type of flow is also important in engineering appliances, such as dealing with polymers in the basics of chemical engineering, and also functions in metallurgy. The concept of movement restricting planes along with velocity, which linearly alters the distance from fixed points on a sheet, is examined by Crane [19]. Recently, a large number of creators have continued to utilize non-Newtonian fluids beyond, and along with, heat and mass transfer [20,21]. Nadeem et al. [22] examined the time autonomies stretching second-grade fluid. Majeed et al. [23] recommended the consequence of suction over a stretching surface for ferromagnetic non-Newtonian fluid flow. The most compelling results regarding micropolar fluid on various stretching surfaces are discussed under the assumptions (see Refs. [24–28]).

In this analysis, we analyzed the combined effects of the Casson micropolar fluid model over a vertical variable stretching Riga sheet. The Brownian motion and thermophoresis are considered to analyze the impacts over the vertical variable stretching Riga sheet in this analysis; thermal and velocity slip impacts are also analyzed. From the above assumptions, the coupled nonlinear PDEs transformed into nonlinear coupled ODEs using the set of suitable transformations. The nonlinear coupled ODEs are solved through numerical techniques along the Runge–Kutta scheme. The combined Casson and micropolar fluid models under the Brownian motion and thermophoresis over a vertical variable stretching Riga sheet is not discussed. When we compared our results to decay results, we found that our results were more suited with decay literature. These results are noteworthy and practical in both engineering and industry. The impacts of pertinent flow parameters on skin friction, the Nusselt number, and temperature and velocity distributions are depicted through tabular form, as well as in graphical form.

2. Flow Formulation

We considered the micropolar–Casson fluid flow with the Buongiorno Model on a vertical Riga sheet (see in Figure 1); the thermal slip and velocity slip were also implemented on the vertical Riga sheet. Heat and mass transportation is explored in the presence of a modified Hartmann number, buoyancy forces, thermophoresis, and Brownian motion. C_w and C_∞ wall concentration corresponded with ambient concentration. u and v are the velocity component along x- and y-direction. T_w and T_∞ are the corresponding wall temperature and ambient temperature. Under the above assumptions, the mathematical

model is developed by means of boundary layer approximation in the form of partial differential equations which is presented below (see Refs. [29–32]):

$$\frac{\partial u}{\partial x} + \frac{\partial v}{\partial y} = 0, \tag{1}$$

$$u\frac{\partial u}{\partial x} + v\frac{\partial u}{\partial y} = \nu\left(1 + \frac{1}{\beta} + K\right)\frac{\partial^2 u}{\partial y^2} + \frac{M_0 J_0}{8\pi\rho} exp\left(-\frac{\pi}{a}\, y\right) + g[\beta(T - T_\infty) + \beta^*(C - C_\infty)] + \frac{K}{\rho}\frac{\partial N}{\partial y}, \tag{2}$$

$$u\frac{\partial N}{\partial x} + v\frac{\partial N}{\partial y} = \frac{\gamma}{\rho_j}\frac{\partial^2 N}{\partial y^2} - \frac{K}{\rho_j}\left(2N + \frac{\partial u}{\partial y}\right), \tag{3}$$

$$u\frac{\partial T}{\partial x} + v\frac{\partial T}{\partial y} = \frac{k_f}{(\rho c_p)_f}\frac{\partial^2 T}{\partial y^2} + g\left[\frac{D_t}{T_\infty}\left(\frac{\partial T}{\partial y}\right)^2 + D_B\frac{\partial C}{\partial y}\frac{\partial T}{\partial y}\right], \tag{4}$$

$$u\frac{\partial C}{\partial x} + v\frac{\partial C}{\partial y} = \frac{D_t}{T_\infty}\frac{\partial^2 T}{\partial y^2} + D_B\frac{\partial^2 C}{\partial y^2}, \tag{5}$$

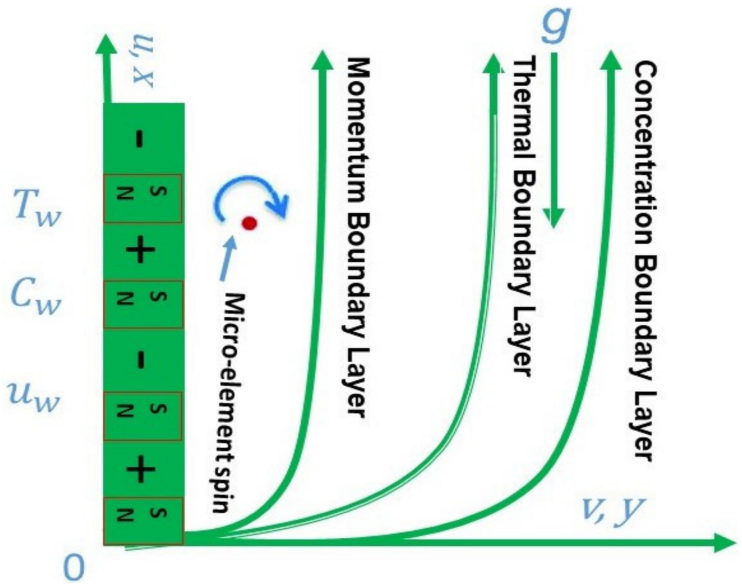

Figure 1. Flow pattern of micropolar–Casson fluid.

The suitable boundary conditions are stated as

$$\begin{cases} u = U_w + \lambda_2\frac{\partial u}{\partial y}, \quad v = 0, \quad N = -m_0\frac{\partial u}{\partial y}, \quad -\lambda^*\frac{\partial T}{\partial y} = T - T_\infty, \quad \frac{\partial C}{\partial y} = -\left(\frac{D_t}{D_B T_\infty}\right)\frac{\partial T}{\partial y}, \\ as\ y \to 0, \\ u \to 0, \quad N \to 0, \quad T \to T_\infty\,, \quad C \to C_\infty\ as\ \ y \to \infty. \end{cases} \tag{6}$$

where the constant m_0 ranges from $0 \le m_0 \le 1$. The concentrated particle flows ($m_0 = 0.0$) cannot rotate due to a strong concentration of elements near the wall surface (Jena and Mathur [6]). When $m_0 = 1/2$, the anti-symmetrical part of the stress tensor vanishes (Ahmadi [7]). In the case of turbulent boundary layer flows, Peddieson [33] suggests that $m_0 = 1$. Introducing the suitable transformations are

$$u = U_w f'(\eta), \ \ v = -\sqrt{\nu a} f(\eta), \ \ \eta = \left(\frac{U_w}{\nu x}\right)y, \ \ \psi = (\nu x U_w\,) f(\eta), \ \ N = U_w\sqrt{\left(\frac{U_w}{\nu x}\right)}g(\eta), \ \ \Phi(\eta) = \frac{T - T_\infty}{T_f - T_\infty}, \ \ R(\eta) = \frac{C - C_\infty}{C_w - C_\infty}. \tag{7}$$

The coupled nonlinear PDEs are changed into connected non-linear ODEs (ordinary differential equations) by adopting the similarity transformations given above. The continuity equation is directly fulfilled by adopting the suitable transformations which are represented as Equation (1) in this paper. The reduced nonlinear system of equations is presented as below:

$$\left(1+K+\frac{1}{\beta_1}\right)f''' - f'^2 + ff'' + Mexp(-\epsilon\eta) + \lambda_t\Phi(\eta) + Kg'(\eta) + \lambda_c R(\eta) = 0, \quad (8)$$

$$\left(1+\frac{K}{2}\right)g'' - f'g + fg' - K(2g+f'') = 0, \quad (9)$$

$$\frac{1}{Pr}\Phi'' + f\Phi' + N_b\Phi'R' + N_t\Phi'^2 = 0, \quad (10)$$

$$R'' + ScfR' + \frac{N_t}{N_b}\Phi'' = 0. \quad (11)$$

With boundary conditions

$$\begin{cases} 1+\lambda f''(0) - f'(0) = 0, \;\; f(0) = 0, \;\; f'(\infty) \to 0, \\ g(0) + m_o f''(0) = 0, \;\; \lambda_1\Phi'(0) + 1 = \Phi(0), \;\; R'(0) + \frac{N_t}{N_b}\Phi'(0) = 0, \\ \Phi(\infty) \to 0, \;\; R(\infty) \to 0. \end{cases} \quad (12)$$

3. Numerical Solution

The highly non-linear connected boundary layer problem of the third-order and the second-order form the Equations (8)–(11)—given the related boundary conditions in Equation (12)—and are solved through a numerical technique using the Matlab software packages. We started with an initial guess value and selected and solved the problems with certain subjective physical parameters to acquire the numerical results. These results are revealed by numerical data as well as in graphical form. The above network of connected nonlinear ODEs (ordinary differential equations) is solved with the help of the Runge–Kutta scheme's built-in strategy. The significant value of the η is chosen for the set of subjective physical parameters. From there, the Runge–Kutta methodology is applied to solve numerically ordinary differential equations. The description of the methodology diagram is provided in Figure 2. The numerical procedure is defined as:

$$\begin{gathered} y(1) = f(\eta), \\ y(2) = f'(\eta), \\ y(3) = f''(\eta), \\ yy1 = f'''(\eta), \\ yy1 = -\left[1+K+\tfrac{1}{\beta}\right]^{-1}(y(2)^2 - y(1)y(3) + Mexp(-\epsilon\eta) + \lambda_c y(8) + \lambda_t y(6) + Ky(5), \\ y(4) = g(\eta) \\ y(5) = g'(\eta), \\ yy2 = g''(\eta), \\ yy2 = -\left(\left(1+\tfrac{K}{2}\right)^{-1}\right)(y(1)y(5) - y(2)y(4) - K(2y(4) + y(3))), \\ y(6) = \Phi(\eta), \\ y(7) = \Phi'(\eta), \\ yy3 = \Phi''(\eta), \\ yy3 = -Pr\big(y(1)y(7) + N_b y(9)y(7) + N_t y(7)^2\big), \\ y(8) = R(\eta), \\ y(9) = R'(\eta), \\ yy4 = -\Big(Scy(1)y(9) + \tfrac{N_t}{N_b}yy3\Big). \end{gathered}$$

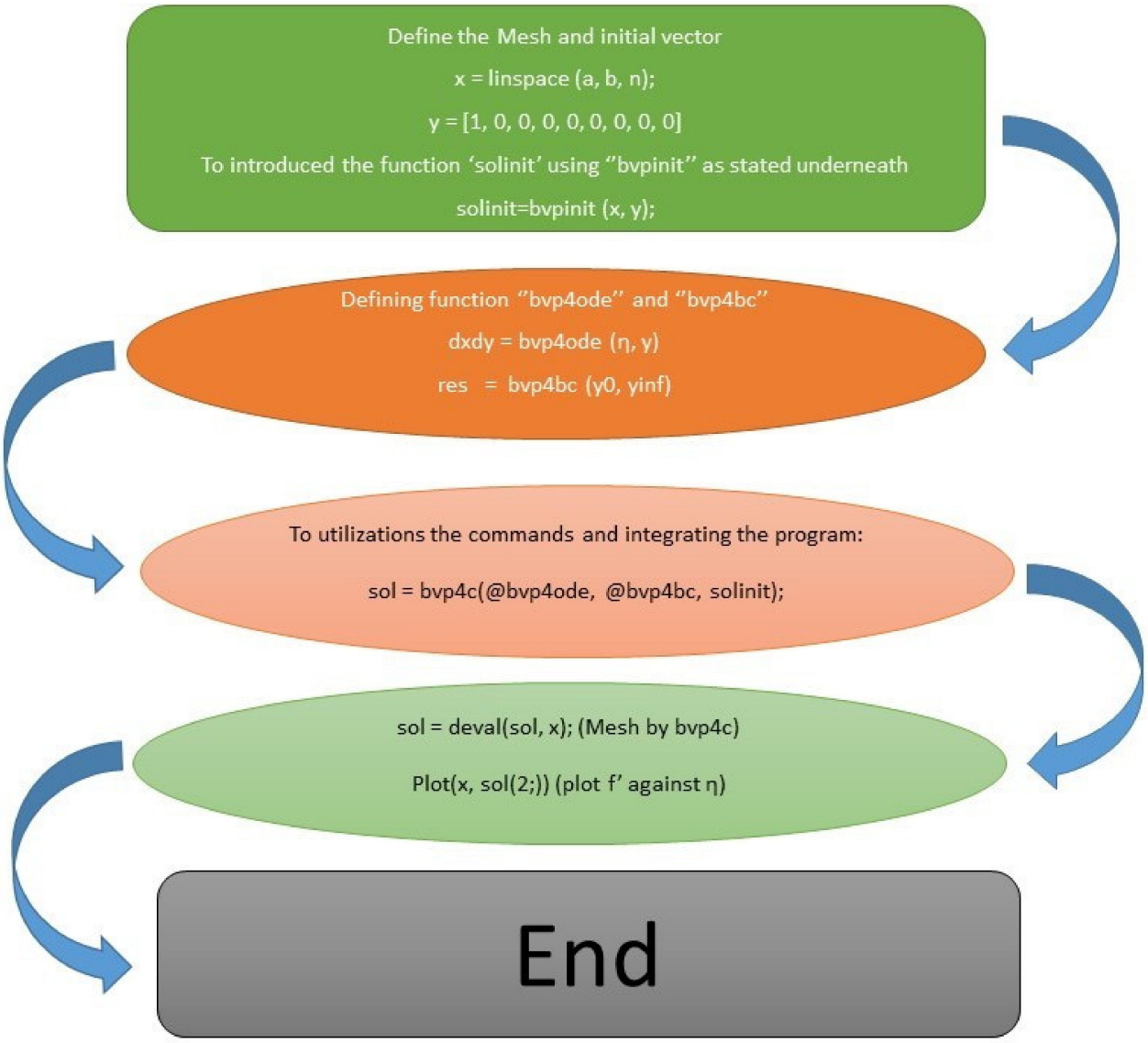

Figure 2. Description of the numerical scheme.

Subject to the boundary conditions

$$y0(1);\ \ 1+\lambda y0(3)-y(2);\ \ y0(4)+m_o y0(3);\ \lambda_1 y0(7)+1-y0(6);$$

$$y0(9)+\frac{N_t}{N_b}y0(7)=0;\ \ yinf(2);\ \ yinf(4);\ \ yinf(6);\ \ yinf(8);$$

The nonlinear higher-order differential system is solved by using the fifth-order Runge–Kutta–Fehlberg scheme. The numerical results will converge if the boundary residuals are less than tolerance error, i.e., 10^{-6}. Introductory approximations are altered with the Newton method and the method is repeated unless it meets the required convergence basis. The boundary residuals are presented as:

$$R_1(u_1,\ u_2,\ u_3,\ u_4\ ) = \ |y_2(\infty)-\widehat{y_2}(\infty)|,$$

$$R_2(u_1,\ u_2,\ u_3,\ u_4\ ) = \ |y_4(\infty)-\widehat{y_4}(\infty)|.$$

$$R_3(u_1,\ u_2,\ u_3,\ u_4\ ) = \ |y_6(\infty)-\widehat{y_6}(\infty)|,$$

$$R_4(u_1,\ u_2,\ u_3,\ u_4\ ) = \ |y_8(\infty)-\widehat{y_8}(\infty)|.$$

Hence, $\widehat{y_2}(\infty)$, $\widehat{y_4}(\infty)$, $\widehat{y_6}(\infty)$, and $\widehat{y_8}(\infty)$ are computed boundary values.

4. Results and Discussion

The impact of the numerous dimensionless parameters of the fluid velocity, micropolar, temperature, and concentration distributions are revealed through graphs and tables. Figures 3–9 show the impacts of the Casson fluid parameter (β_1), dimensionless parameter (ε), micropolar parameter (K), buoyancy parameters (λ_c and λ_t), velocity slip (λ), and modified the Hartman number (M) on the fluid velocity distribution $(F'(\zeta))$. The influence of Casson fluid parameter (β_1) on fluid velocity distribution $(F'(\zeta))$ is presented in Figure 3. The increment of Casson fluid parameter (β_1) declined the fluid velocity. The momentum thickness was physically enhanced due to the increment of the Casson fluid parameter (β_1). The influence of the dimensionless parameter (ε) on fluid velocity distribution $(F'(\zeta))$ is expressed in Figure 4. The curves of fluid velocity distribution declined due to the increment of the dimensionless parameter (ε). Physically, the distance from the sheet to magnetic fields declined exponentially, which ultimately reduced the fluid velocity function. The impact of the micropolar parameter (K) on fluid velocity distribution $(F'(\zeta))$ is exhibited in Figure 5. The fluid velocity distribution curves show increasing behavior due to increments of the micropolar parameter (K) due to the increase in the rotation of the fluid the velocity of fluid increased. Figures 6 and 7 reveal the indication of buoyancy force parameters (λ_c and λ_t) on fluid velocity distribution $(F'(\zeta))$. The fluid velocity distribution $(F'(\zeta))$ and buoyancy force parameters (λ_c and λ_t) revealed similar increasing behavior due to the increased gravity force, which developed pressure and led to enhanced fluid velocity distribution near the surface. Figure 8 exhibits the effect of the velocity slip (λ) on fluid velocity distribution $(F'(\zeta))$. The reduction in curves of fluid velocity distribution $(F'(\zeta))$ is revealed due to the increment in velocity slip (λ). The velocity slip (λ) is increased, which causes a decline in the thickness of velocity distribution. The effect of the modified Hartman number (M) on the fluid velocity distribution $(F'(\zeta))$ is presented in Figure 9. The increment in the modified Hartman number (M) increased the momentum boundary layer thickness. The modified Hartmann number is the relation between electromagnetic and viscous forces; as the viscous forces declined, fluid velocity and electromagnetic force increased. Figure 10 shows the influence of micropolar parameter (K) on micropolar distribution $(g(\zeta))$. The curves of micropolar distribution $(g(\zeta))$ are enhanced due to an increment of the micropolar parameter (K) ; the rotation of the fluid parameter increased and enhanced the micropolar fluid distribution. Figures 11–13 indicate the influence of thermal slip (λ_1), Brownian motion (N_b), and thermophoresis (N_t) parameters on temperature distribution $(\phi(\zeta))$. Figure 11 connects the impact of thermal slip (λ_1) on the temperature distribution $(\phi(\zeta))$. The curves of temperature distribution $(\phi(\zeta))$ decline due to the enhancement in thermal slip (λ_1). The increment in thermal slip physically declined because the surface drag led to a decline in the production of heat amount and reduced the temperature distribution. Figure 12 communicates the impacts of Brownian motion (N_b) on the temperature distribution $(\phi(\zeta))$. The curves of temperature distribution $(\phi(\zeta))$ show declined behavior due to the enhancement in Brownian motion (N_b). According to Brownian motion, the nanoparticles in fluid transfer randomly. In addition to accelerating the collision between nanoparticles and fluid molecules, this random movement also converts the kinetic energy of molecules into thermal energy, which increased the temperature profile. Figure 13 indicates the influence of thermophoresis (N_t) on temperature distribution $(\phi(\zeta))$. Increments in the thermophoresis (N_t) parameter declined the curves of temperature distribution $(\phi(\zeta))$, causing nanofluid particles suspended in the fluid to migrate through the direction of the declining temperature of fluid. Figures 14–16 indicate the influence of Brownian motion (N_b), thermophoresis (N_t), and Schmidt number (Sc) parameters on concentration distribution $(R(\zeta))$. Figure 14 indicates the influence of Brownian motion (N_b) on concentration distribution $(R(\zeta))$. Increments in Brownian motion (N_b), which declined the curves of concentration distribution $(R(\zeta))$, increased curves of temperature distribution $(\phi(\zeta))$ after point of intersection. The influence of ther-

mophoresis (N_t) on concentration distribution ($R(\zeta)$) is indicated in Figure 15. Increments in thermophoresis (N_t) increased the curves of concentration distribution ($R(\zeta)$)because the particles increased; the concentration profile also increased, but the curves of concentration distribution reduced ($R(\zeta)$) after the point of intersection. Figure 16 indicates the influence of the Schmidt number (Sc) on concentration distribution ($R(\zeta)$). Increments in the Schmidt number (Sc) caused a decline in the curves of concentration distribution ($R(\zeta)$) but increased curves of concentration distribution ($R(\zeta)$) after point of intersection.

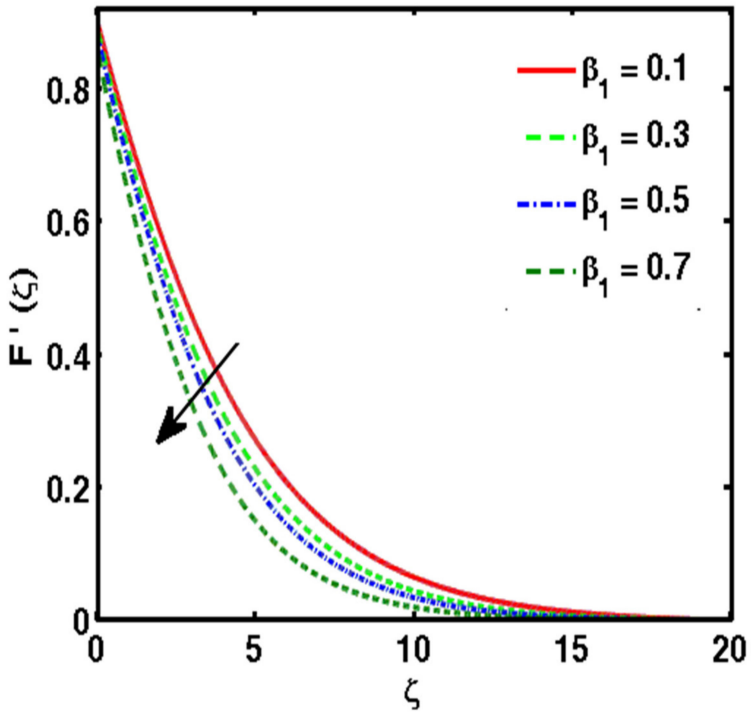

Figure 3. Variation of β_1 and $F'(\zeta)$.

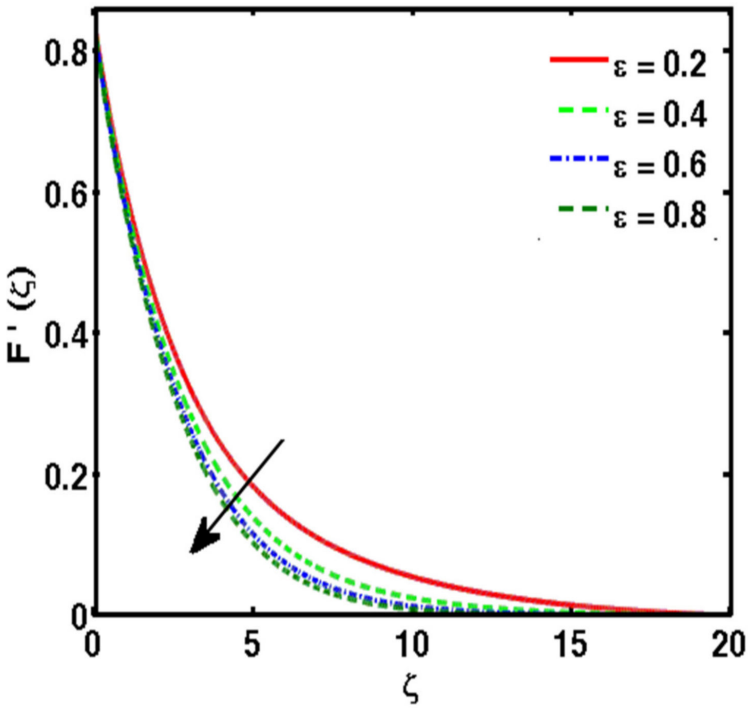

Figure 4. Variation of ε and $F'(\zeta)$.

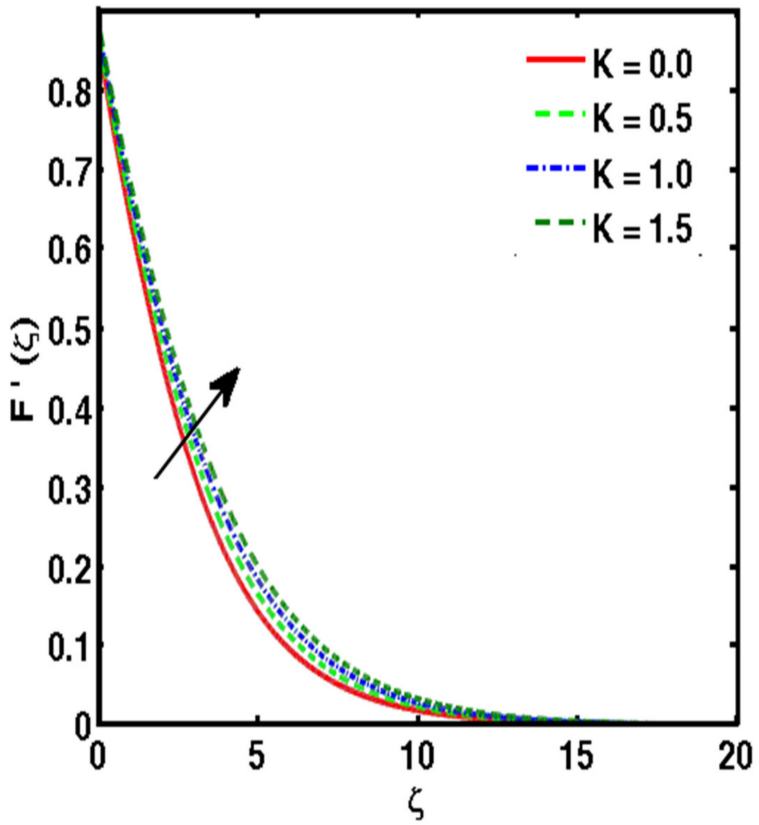

Figure 5. Variation of K and $F'(\zeta)$.

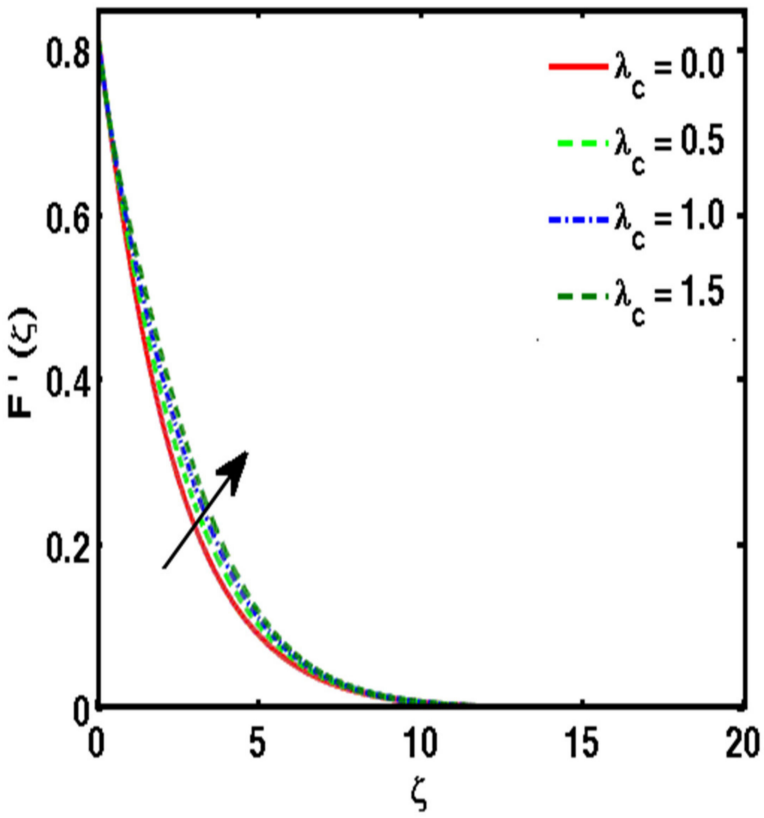

Figure 6. Variation of λ_c and $F'(\zeta)$.

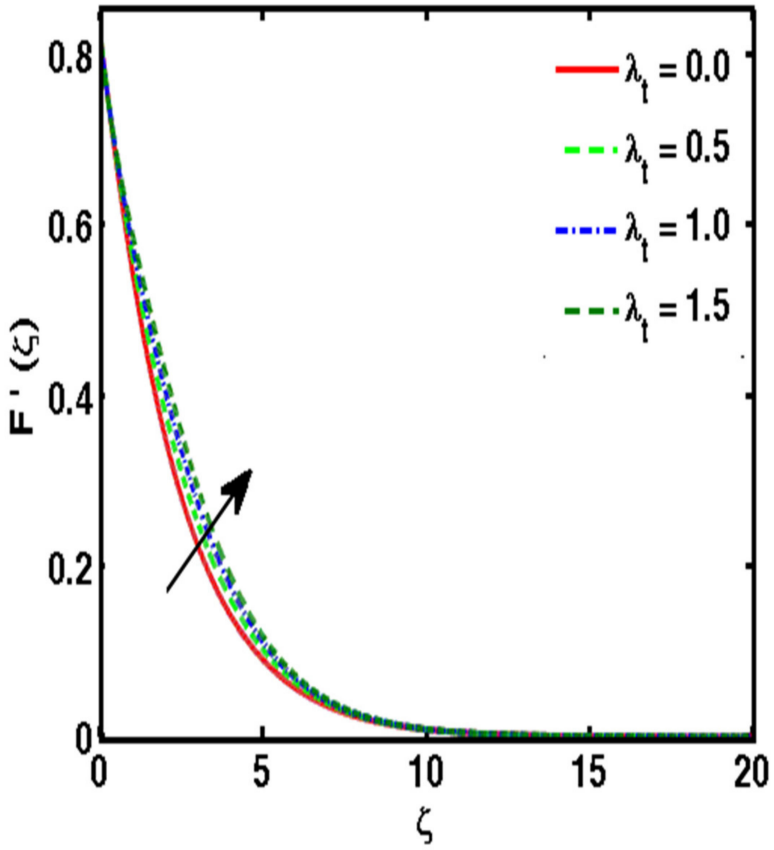

Figure 7. Variation of λ_t and $F'(\zeta)$.

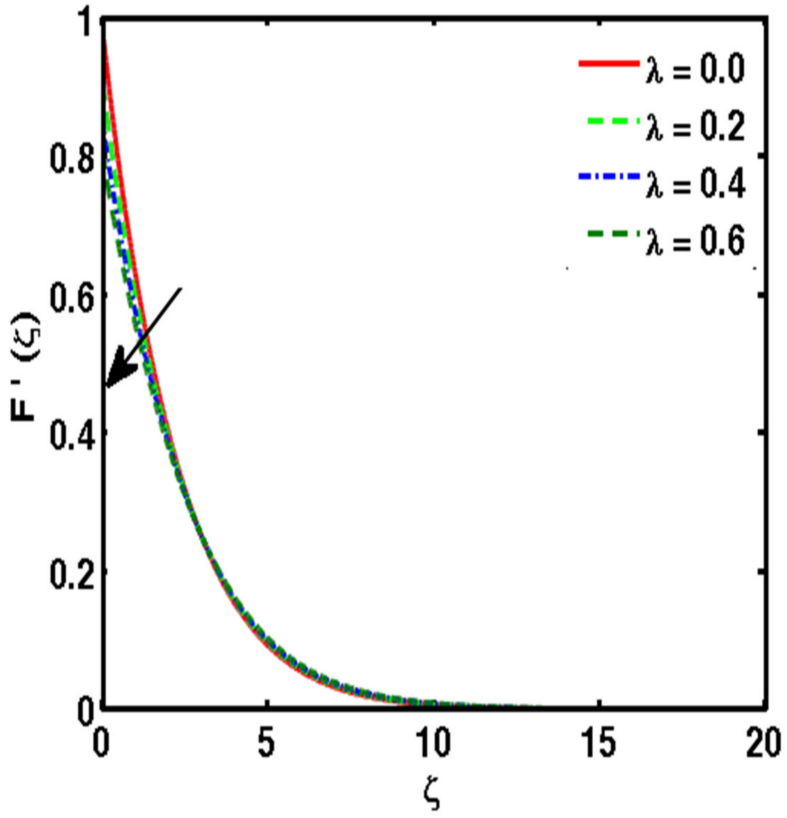

Figure 8. Variation of λ and $F'(\zeta)$.

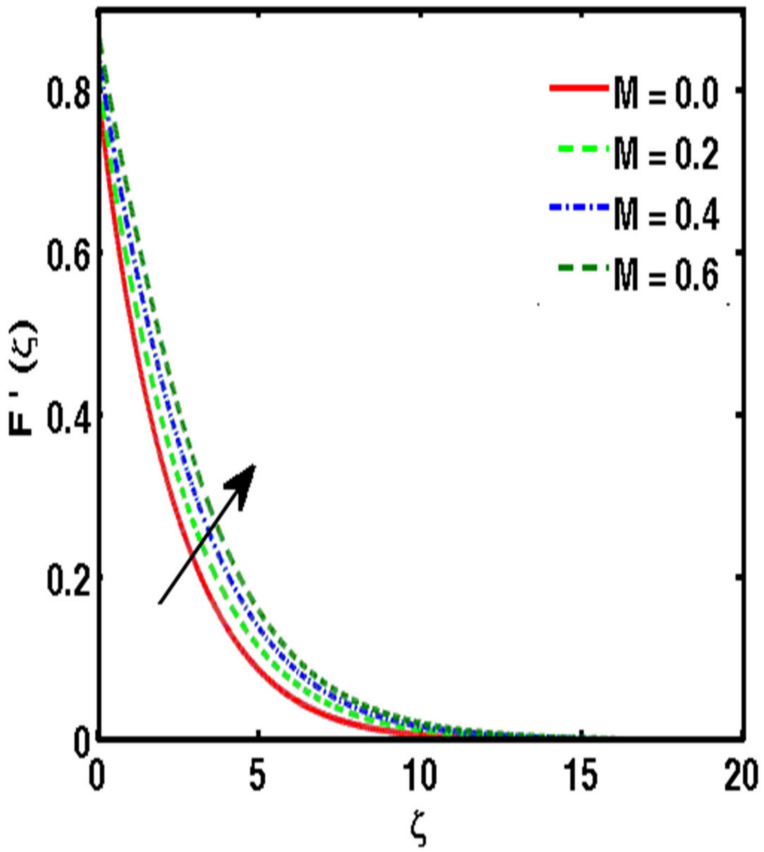

Figure 9. Variation of M and $F'(\zeta)$.

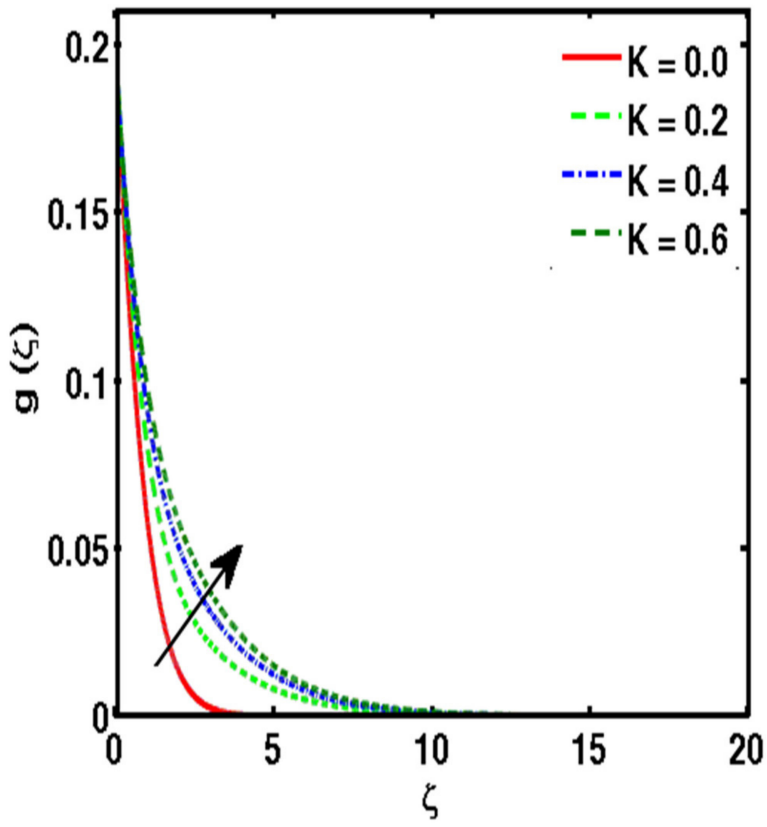

Figure 10. Variation of K and $F\prime(\zeta)$.

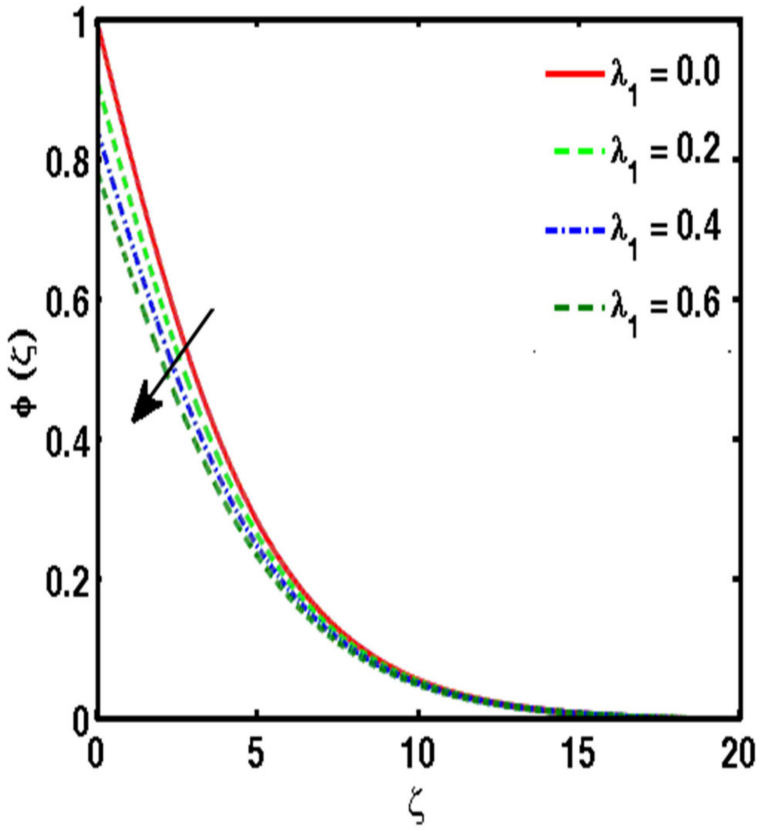

Figure 11. Variation of λ_1 and $\phi(\zeta)$.

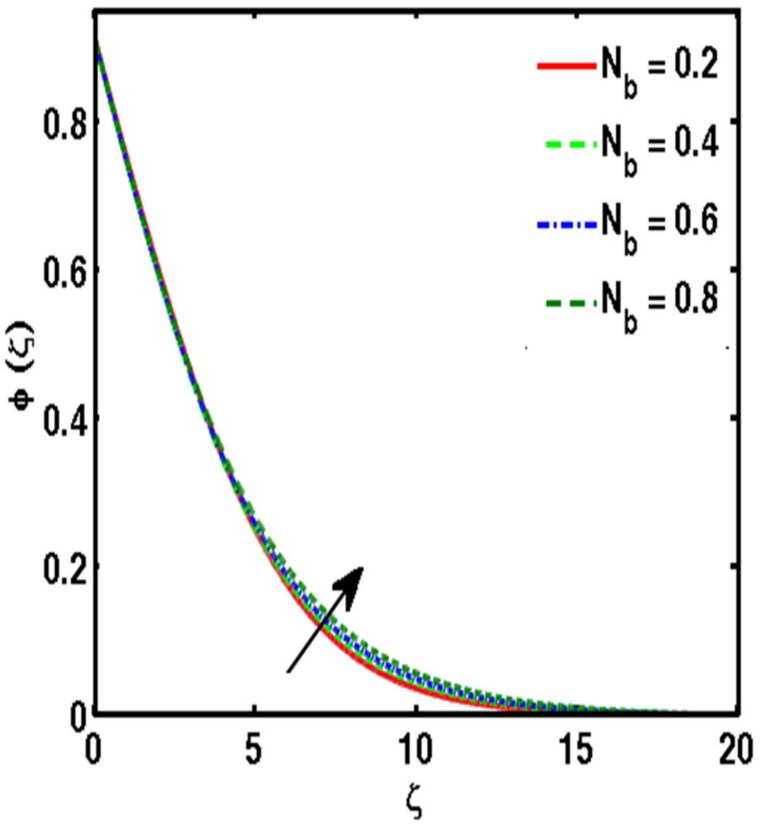

Figure 12. Variation of N_b and $\phi(\zeta)$.

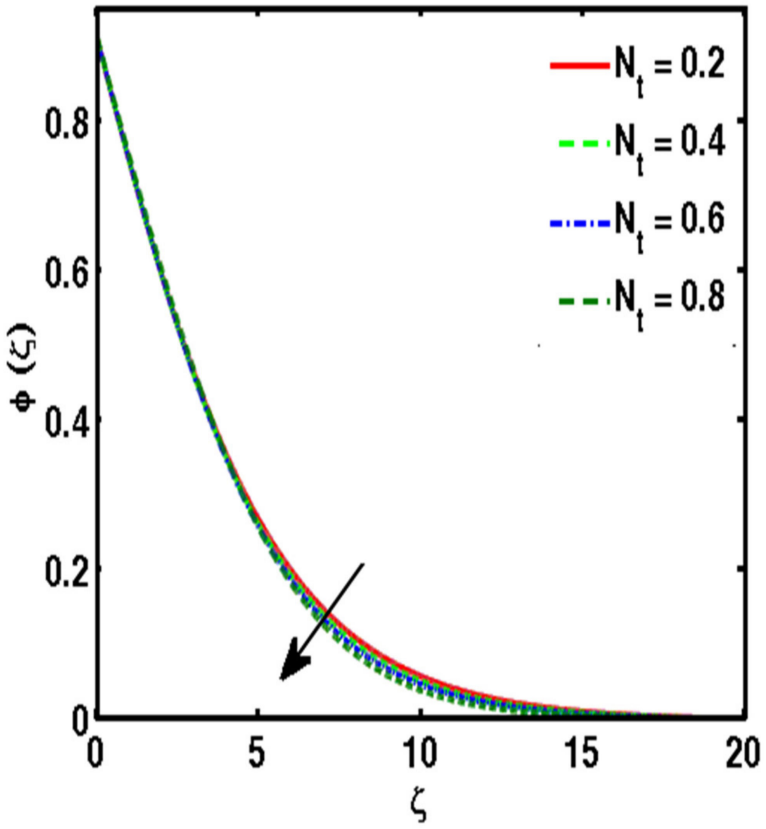

Figure 13. Variation of N_t and $\phi(\zeta)$.

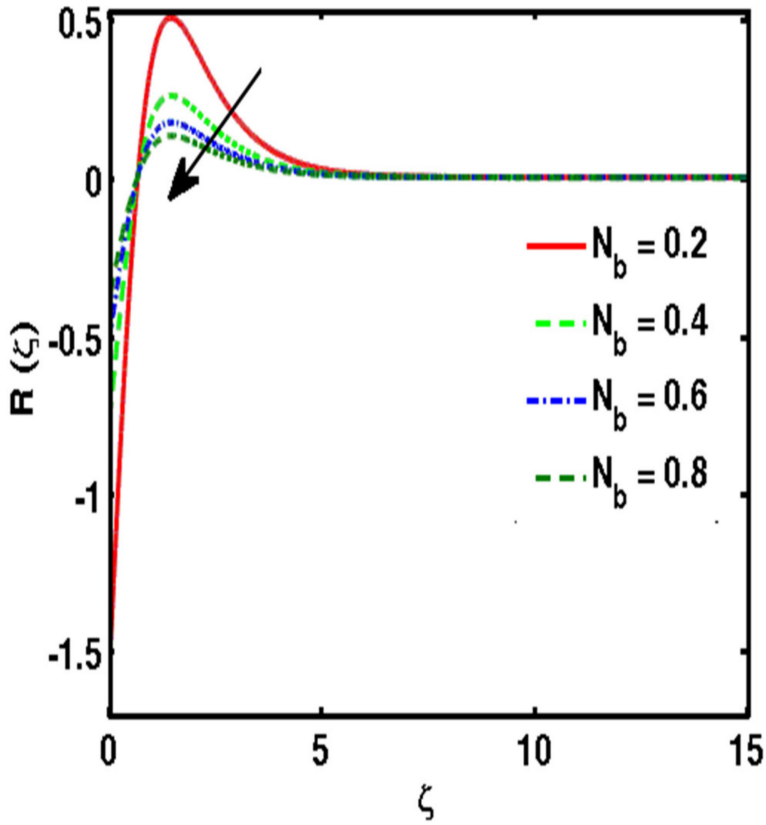

Figure 14. Variation of N_b and $R(\zeta)$.

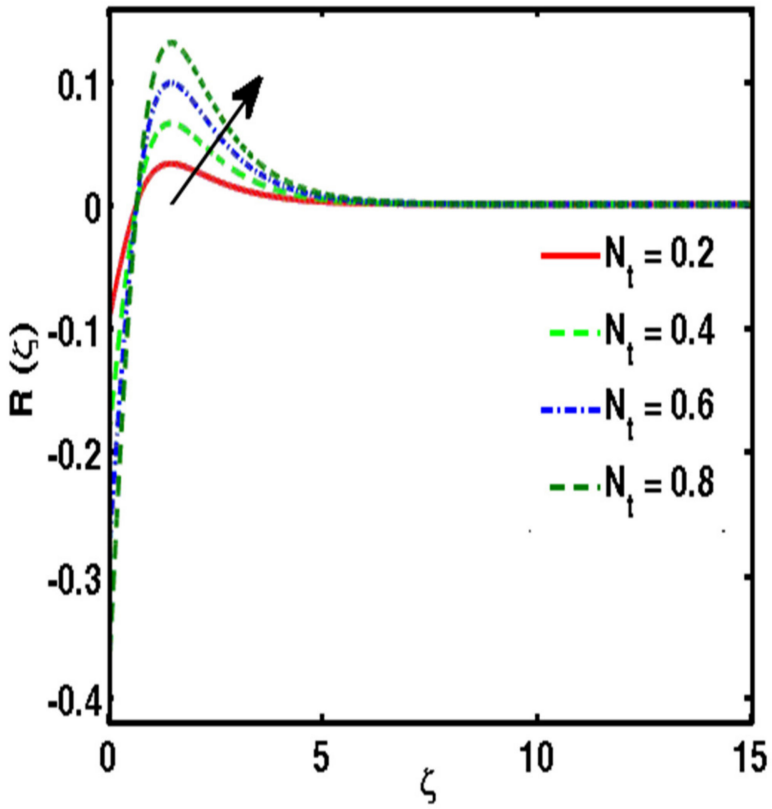

Figure 15. Variation of N_t and $R(\zeta)$.

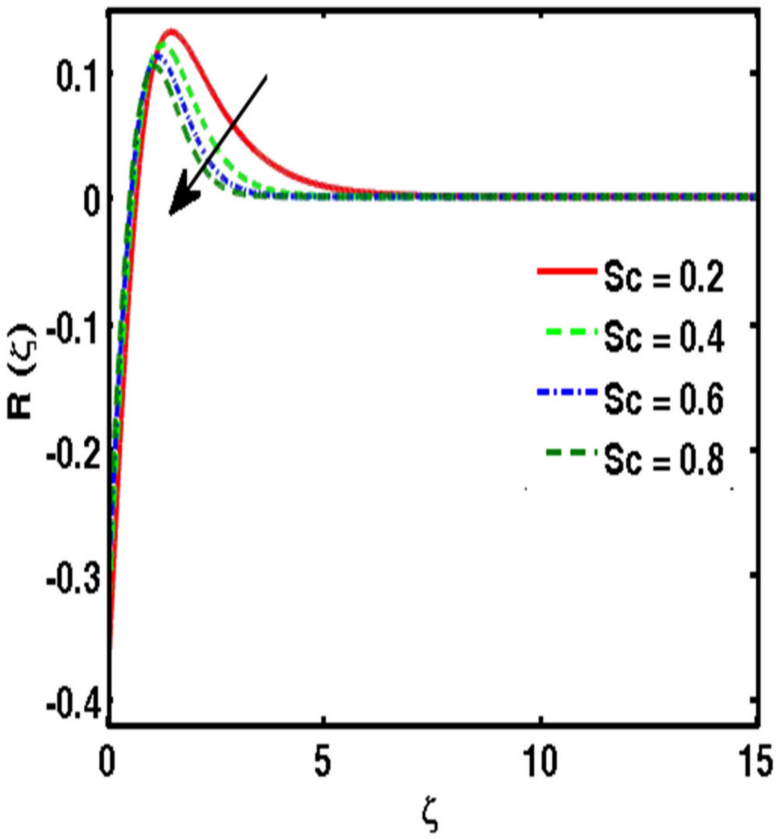

Figure 16. Description of the numerical scheme.

Table 1 indicates the effects of the Casson fluid parameter (β_1), dimensionless parameter (ε), buoyancy parameters (λ_c and λ_t), micropolar parameter (K), modified Hartman number (M), and velocity slip (λ) on skin friction $(C_f Re^{\frac{1}{2}})$ for both weak $(m_0 = 0.5)$ and strong $(m_0 = 0.0)$ cases of concentration. Increment in the Casson fluid parameter declined skin friction in both weak $(m_0 = 0.5)$ and strong $(m_0 = 0.0)$ concentration cases. Table 1 indicates the impact of the dimensionless parameters on skin friction $(C_f Re^{\frac{1}{2}})$. The skin friction $(C_f Re^{\frac{1}{2}})$ and dimensionless parameter have the same growing behavior; physically, the distance from surface to magnetic field declines exponentially and ultimately enhances the skin friction. The impression of buoyancy force parameters (λ_c and λ_t) on skin friction is exhibited in Table 1. The increment in λ_t is increased skin friction $(C_f Re^{\frac{1}{2}})$; however, λ_c and skin friction $(C_f Re^{\frac{1}{2}})$ have been found to behave oppositely. The influence of the micropolar parameter (K) on skin friction $(C_f Re^{\frac{1}{2}})$ is indicated in Table 1. Micropolar parameters (K) and skin friction $(C_f Re^{\frac{1}{2}})$ are found to be an increasing behavior. Rotation of fluid also increased, which, in turn, increased the friction between surface and fluid. Table 1 indicates the effects of the modified Hartman number (M) on skin friction $(C_f Re^{\frac{1}{2}})$; the impression shows that the modified Hartman number (M) and skin friction $(C_f Re^{\frac{1}{2}})$ have opposite performances. The modified Hartmann number is the relation between electromagnetic and viscous forces; as the viscous forces declined, the electromagnetic force increased and skin friction declined. Table 1 indicates the effects of velocity slip (λ) on skin friction $(C_f Re^{\frac{1}{2}})$. The impression shows that velocity slip (λ) and skin friction $(C_f Re^{\frac{1}{2}})$ have opposite performances. The velocity slip is the contact point for the ratio of fluid and surface. As the skin friction declined, the velocity slip increased. Table 2 indicates the impacts of Brownian motion (N_b), thermophoresis (N_t), Schmidt number (Sc), thermal slip (λ_1), Casson fluid parameter (β_1), and micropolar parameter (K) on the Sherwood number $(Sh_x Re^{\frac{1}{2}})$ and Nusselt number $(Nu_x Re^{\frac{1}{2}})$. The impact of Brownian motion (N_b) on the Sherwood number $(Sh_x Re^{\frac{1}{2}})$ and Nusselt number $(Nu_x Re^{\frac{1}{2}})$, which are presented in Table 2, show that Brownian motion (N_b) and the magnitude of the Sherwood number $(Sh_x Re^{\frac{1}{2}})$ have opposite performances; the Nusselt number $(Nu_x Re^{\frac{1}{2}})$ and Brownian motion (N_b) also have opposite performances in cases of both weak $(m_0 = 0.5)$ and strong $(m_0 = 0.0)$ concentration. The Sherwood number $(Sh_x Re^{\frac{1}{2}})$ and Nusselt number $(Nu_x Re^{\frac{1}{2}})$ show successively higher values in case of strong $(m_0 = 0.0)$ concentration as compared to weak concentration $(n = 0.5)$. In addition to accelerating the collision between nanoparticles and fluid molecules, this random movement also converts molecules' kinetic energy into thermal energy, which reduced both the Nusselt number and Sherwood number. The impact of thermophoresis (N_t) on the Sherwood number $(Sh_x Re^{\frac{1}{2}})$ and Nusselt number $(Nu_x Re^{\frac{1}{2}})$ is presented in Table 2. Thermophoresis (N_t) and the magnitude of the Sherwood number $(Sh_x Re^{\frac{1}{2}})$ both increase, while the Nusselt number $(Nu_x Re^{\frac{1}{2}})$ and thermophoresis (N_t) have opposite performances in cases of both weak $(m_0 = 0.5)$ and strong $(m_0 = 0.0)$ concentration. The Sherwood number $(Sh_x Re^{\frac{1}{2}})$ and Nusselt number $(Nu_x Re^{\frac{1}{2}})$ showed higher values in case of strong $(m_0 = 0.0)$ concentration as compared to weak $(m_0 = 0.5)$ concentration. Increments in the thermophoresis (N_t) parameter declined with the Nusselt number. Nanofluid particles suspended in the fluid migrate through the direction of decline with the Nusselt number but react oppositely with the thermophoresis parameter. The influence of the Schmidt number (Sc) on the Sherwood number $(Sh_x Re^{\frac{1}{2}})$ and Nusselt number $(Nu_x Re^{\frac{1}{2}})$ is indicated in Table 2. The values of the Sherwood number $(Sh_x Re^{\frac{1}{2}})$ and Nusselt number $(Nu_x Re^{\frac{1}{2}})$ both decline due to increments in the Schmidt number (Sc). The Sherwood number $(Sh_x Re^{\frac{1}{2}})$ and Nusselt number $(Nu_x Re^{\frac{1}{2}})$ show higher values in cases of strong $(m_0 = 0.0)$ concentration as compared to weak $(m_0 = 0.5)$ concentration. Variations in thermal slip (λ_1), Sherwood number $(Sh_x Re^{\frac{1}{2}})$, and Nusselt number $(Nu_x Re^{\frac{1}{2}})$ are shown in Table 2. It is noted that thermal slip (λ_1) and the magnitude of the Sherwood

number ($Sh_xRe^{\frac{1}{2}}$) and Nusselt number ($Nu_xRe^{\frac{1}{2}}$) have opposite performance in both cases of weak ($m_0 = 0.5$) and strong ($m_0 = 0.0$) concentrations. Variations of the Casson fluid parameter (β_1) and Sherwood number ($Sh_xRe^{\frac{1}{2}}$) and Nusselt number ($Nu_xRe^{\frac{1}{2}}$) are shown in Table 2. The Casson fluid parameter (β_1) and the magnitude of both the Sherwood number ($Sh_xRe^{\frac{1}{2}}$) and Nusselt number ($Nu_xRe^{\frac{1}{2}}$) have opposite performance in both cases of weak ($m_0 = 0.5$) and strong ($m_0 = 0.0$) concentration as the shear-thinning is increased, which declines with the Sherwood number ($Sh_xRe^{\frac{1}{2}}$) and Nusselt number ($Nu_xRe^{\frac{1}{2}}$). The indications of the micropolar parameter (K), Sherwood number ($Sh_xRe^{\frac{1}{2}}$) and Nusselt number ($Nu_xRe^{\frac{1}{2}}$) are shown in Table 2. It is noted that micropolar parameter (K) and magnitude of both the Sherwood number ($Sh_xRe^{\frac{1}{2}}$) and Nusselt number ($Nu_xRe^{\frac{1}{2}}$) have similar increases in cases of both weak ($m_0 = 0.5$) and strong ($m_0 = 0.0$) concentration. Table 3 is provided the comparison of results with two different techniques—bvp4c and NDsolve—for different values of β_1 and ε while the rest of physical parameters remained fixed, which was found to be in agreement with other results. Table 4 is presented the comparison of our results with Khan and Pop [34], Wang [35], and Gorla and Sidawi [36] when the rest of the physical parameters were considered zero. Our results are in agreement with decay results.

Table 1. Numerical results of skin friction for different values of parameters.

Physical Parameters							$C_fRe^{\frac{1}{2}}$	
β_1	ε	λ_t	λ_c	K	M	λ	$m_0 = 0.0$	$m_0 = 0.5$
0.2	0.3	0.4	0.5	0.6	0.4	0.2	−1.673226	−1.725221
0.4	-	-	-	-	-	-	−1.214027	−1.270021
0.6	-	-	-	-	-	-	−1.037617	−1.095173
0.8	-	-	-	-	-	-	−0.9431868	−1.001566
0.4	0.1	-	-	-	-	-	−1.022292	−1.069329
-	0.3	-	-	-	-	-	−1.214027	−1.270021
-	0.5	-	-	-	-	-	−1.315013	−1.375856
-	0.7	-	-	-	-	-	−1.375353	−1.439143
-	0.3	0.0	-	-	-	-	−1.310721	−1.371746
-	-	0.2	-	-	-	-	−1.262185	−1.320671
-	-	0.4	-	-	-	-	−1.214027	−1.270021
-	-	0.6	-	-	-	-	−1.166235	−1.219783
-	-	0.4	0.0	-	-	-	−1.200159	−1.255625
-	-	-	0.5	-	-	-	−1.214027	−1.270021
-	-	-	1.0	-	-	-	−1.229498	−1.28614
-	-	-	1.5	-	-	-	−1.241787	−1.303813
-	-	-	0.5	0.0	-	-	−1.103828	−1.103828
-	-	-	-	0.3	-	-	−1.162278	−1.189609
-	-	-	-	0.6	-	-	−1.214027	−1.270021
-	-	-	-	0.9	-	-	−1.262202	−1.34753
-	-	-	-	0.6	0.0	-	−1.649318	−1.726431
-	-	-	-	-	0.2	-	−1.426766	−1.492998
-	-	-	-	-	0.4	-	−1.214027	−1.270021

Table 1. *Cont.*

Physical Parameters							$C_f Re^{\frac{1}{2}}$	
β_1	ε	λ_t	λ_c	K	M	λ	$m_0 = 0.0$	$m_0 = 0.5$
-	-	-	-	-	0.6	-	−1.008469	−1.054712
-	-	-	-	-	0.4	0.0	−1.397646	−1.472076
-	-	-	-	-	-	0.2	−1.214027	−1.270021
-	-	-	-	-	-	0.4	−1.075704	−1.119696
-	-	-	-	-	-	0.6	−0.9672141	−1.002867

Table 2. Numerical results of the Sherwood number and Nusselt number for different values of parameters.

Physical Parameters						$m_0 = 0.0$		$m_0 = 0.5$	
N_b	N_t	Sc	λ_1	β_1	K	$Nu_x Re^{\frac{1}{2}}$	$Sh_x Re^{\frac{1}{2}}$	$Nu_x Re^{\frac{1}{2}}$	$Sh_x Re^{\frac{1}{2}}$
0.2	0.4	0.5	0.5	0.4	0.6	0.7248814	−1.449763	0.7232926	−1.446585
0.4	-	-	-	-	-	0.724467	−0.724467	0.7228847	−0.7228847
0.6	-	-	-	-	-	0.7243141	−0.4828761	0.7227331	−0.4818221
0.8	-	-	-	-	-	0.7242348	−0.3621174	0.7226542	−0.3613271
0.4	0.2	-	-	-	-	0.7282771	−0.3641386	0.726704	−0.363352
-	0.4	-	-	-	-	0.724467	−0.724467	0.7228847	−0.7228847
-	0.6	-	-	-	-	0.7205841	−1.080876	0.7189916	−1.078487
-	0.8	-	-	-	-	0.716627	−1.433254	0.7150231	−1.430046
-	0.4	0.0	-	-	-	0.7290085	−0.7290085	0.727124	−0.727124
-	-	0.5	-	-	-	0.724467	−0.724467	0.7228847	−0.7228847
-	-	1.0	-	-	-	0.7177105	−0.7177105	0.7161199	−0.7161199
-	-	1.5	-	-	-	0.7119261	−0.7119261	0.7103585	−0.7103585
-	-	0.5	0.1	-	-	1.015862	−1.015862	1.012863	−1.012863
-	-	-	0.3	-	-	0.8460207	−0.8460207	0.8438948	−0.8438948
-	-	-	0.5	-	-	0.724467	−0.724467	0.7228847	−0.7228847
-	-	-	0.7	-	-	0.6332804	−0.6332804	0.6320583	−0.6320583
-	-	-	0.5	0.2	-	0.7308407	−0.7308407	0.7299368	−0.7299368
-	-	-	-	0.4	-	0.724467	−0.724467	0.7228847	−0.7228847
-	-	-	-	0.6	-	0.7212873	−0.7212873	0.7192414	−0.7192414
-	-	-	-	0.8	-	0.7193347	−0.7193347	0.7169546	−0.7169546
-	-	-	-	0.4	0.0	0.7219191	−0.7219191	0.7219191	−0.7219191
-	-	-	-	-	0.3	0.7232098	−0.7232098	0.7223637	−0.7223637
-	-	-	-	-	0.6	0.724467	−0.724467	0.7228847	−0.7228847
-	-	-	-	-	0.9	0.7256365	−0.7256365	0.7234127	−0.7234127

Table 3. Comparison of results with two different techniques (bvp4c and NDsolve) for β_1 and ε while the rest of physical parameters remained fixed.

		bvp4c Method		**ND-Solve Method**	
Physical Parameters		$C_f Re^{\frac{1}{2}}$		$C_f Re^{\frac{1}{2}}$	
β_1	ε	$m_0 = 0.0$	$m_0 = 0.5$	$m_0 = 0.0$	$m_0 = 0.5$
0.2	0.3	−1.673226	−1.725221	−1.664712	−1.7246872
0.4	-	−1.214027	−1.270021	−1.205987	−1.2687431
0.6	-	−1.037617	−1.095173	−1.0368794	−1.0946261
0.8	-	−0.9431868	−1.001566	−0.924786	−1.0014782
0.4	0.1	−1.022292	−1.069329	−1.021578	−1.068673
-	0.3	−1.214027	−1.270021	−1.208762	−1.270011
-	0.5	−1.315013	−1.375856	−1.308763	−1.375632
-	0.7	−1.375353	−1.439143	−1.368974	−1.375632

Table 4. The comparison results of Khan and Pop [34], Wang [35], and Gorla and Sidawi [36] with present analysis when the rest of the physical parameters were considered zero.

Pr	**Khan and Pop [34]**	**Wang [35]**	**Gorla and Sidawi [36]**	**Present Analysis**
0.70	0.45390	0.45390	0.53490	0.4538741
2.00	0.91130	0.91140	0.91140	0.9113825
7.00	1.89540	1.89540	1.89050	1.89538941
20.00	3.35390	3.35390	3.35390	3.3537654
70.00	6.46210	6.46220	6.46220	6.4621698

5. Final Remarks

The investigation of micropolar Casson nanofluid flow with thermal and velocity slip over vertical Riga stretching surfaces has been discussed in this study. Significant effects of physical parameters, namely the Casson fluid parameter (β_1), dimensionless parameter (ε), micropolar parameter (K), buoyancy parameters $(\lambda_c$ and $\lambda_t)$, velocity slip (λ), Brownian motion (N_b), thermophoresis (N_t), Schmidt number (Sc), thermal slip (λ_1), and modified Hartman number (M) on the fluid velocity distribution $(F'(\zeta))$, temperature distribution $(\phi(\zeta))$, concentration distribution $(R(\zeta))$, micropolar distribution $(g(\zeta))$, Sherwood number $(Sh_x Re^{\frac{1}{2}})$, skin friction $(C_f Re^{\frac{1}{2}})$, and Nusselt number $(Nu_x Re^{\frac{1}{2}})$ are presented through graphs and tabular form. Some useful results are discussed below:

- The increment of the Casson fluid parameter (β_1) declined with the fluid velocity; thus, thickness is reduced due to the increment of the Casson fluid parameter (β_1);
- Fluid velocity distribution curves show increasing behavior due to increments of the micropolar parameter (K);
- The reduction in curves of fluid velocity distribution $(F'(\zeta))$ is revealed due to the increment in velocity slip (λ);
- The curves of temperature distribution $(\phi(\zeta))$ show declining behavior due to enhancement in Brownian motion (N_b);
- Increments in Brownian motion (N_b) led to declining curves of concentration distribution $(R(\zeta))$; increased curves of concentration distribution $(R(\zeta))$ were found after the point of intersection;
- The curves of temperature distribution $(\phi(\zeta))$ show declining behavior due to an enhancement in Brownian motion (N_b);

- Brownian motion (N_b) and the magnitude of the Sherwood number have opposite performances; Nusselt number and Brownian motion (N_b) also have opposite performance in cases of both weak ($m_0 = 0.5$) and strong ($m_0 = 0.0$) concentration. The Sherwood number and Nusselt number achieved higher values in cases of strong ($m_0 = 0.0$) concentration;
- Thermophoresis (N_t) and the magnitude of the Sherwood number show similar behavior; Nusselt number and thermophoresis (N_t) have opposite performances in cases of both weak ($m_0 = 0.5$) and strong ($m_0 = 0.0$) concentration. The Sherwood number and Nusselt number showed higher values in cases of strong ($m_0 = 0.0$) concentration when compared to cases of weak ($m_0 = 0.5$) concentration.

Author Contributions: N.A. wrote the manuscript under the supervision of W.S. All authors have read and agreed to the published version of the manuscript.

Funding: The authors would like to acknowledge the support of Prince Sultan University for paying the Article Processing Charges (APC) of this publication.

Institutional Review Board Statement: Not applicable.

Informed Consent Statement: Not applicable.

Data Availability Statement: The manuscript included all required data and implementing information.

Acknowledgments: We are thankful to the anonymous referees for their valuable comments, which helped us improve the paper's quality. The authors wish to express their gratitude to Prince Sultan University for facilitating the publication of this article through the research lab Theoretical and Applied Sciences Lab.

Conflicts of Interest: The authors declare no potential conflict of interest with respect to the research, authorship, and/or publication of this article.

Nomenclature

β_1	Casson fluid parameter
ε	Dimensionless parameter
λ_c and λ_t	Buoyancy force parameters
K	Micropolar parameter
M	Modified Hartman number
λ	Velocity slip
N_b	Brownian motion
N_t	Thermophoresis
$C_f Re^{\frac{1}{2}}$	Skin friction
$Nu_x Re^{\frac{1}{2}}$	Nusselt number
u, v	Velocity components
Sc	Schimdt number
λ_1	Thermal slip
C_∞	Ambient concentration
T_∞	Ambient temperature
T_w	Wall temperature
$R(\zeta)$	Concentration distribution
$\phi(\zeta)$	Temperature distribution
$F'(\zeta)$	Velocity distribution
$Sh_x Re^{\frac{1}{2}}$	Sherwood number
$g(\zeta)$	Micropolar distribution
C_∞	Wall concentration

References

1. Eringen, A.C. Theory of micropolar fluids. *J. Math. Mech.* **1966**, *16*, 1–18. [CrossRef]
2. Eringen, A.C. Theory of thermomicrofluids. *J. Math. Anal. Appl.* **1972**, *38*, 480–496. [CrossRef]
3. Ariman TT, N.D.; Turk, M.A.; Sylvester, N.D. Applications of microcontinuum fluid mechanics. *Int. J. Eng. Sci.* **1974**, *12*, 273–293. [CrossRef]
4. Lukaszewicz, G. *Micropolar Fluids: Theory and Applications*; Springer Science & Business Media: Berlin/Heidelberg, Germany, 1999.
5. Eringen, A.C. *Microcontinuum Field Theories: II. Fluent Media*; Springer Science & Business Media: Berlin/Heidelberg, Germany, 2001; Volume 2.
6. Ahmadi, G. Self-similar solution of imcompressible micropolar boundary layer flow over a semi-infinite plate. *Int. J. Eng. Sci.* **1976**, *14*, 639–646. [CrossRef]
7. Jena, S.K.; Mathur, M.N. Similarity solutions for laminar free convection flow of a thermomicropolar fluid past a non-isothermal vertical flat plate. *Int. J. Eng. Sci.* **1981**, *19*, 1431–1439. [CrossRef]
8. Gorla RS, R.; Lin, P.P.; An-Jen, Y. Asymptotic boundary layer solutions for mixed convection from a vertical surface in a micropolar fluid. *Int. J. Eng. Sci.* **1990**, *28*, 525–533. [CrossRef]
9. Bhargava, R.; Kumar, L.; Takhar, H.S. Finite element solution of mixed convection micropolar flow driven by a porous stretching sheet. *Int. J. Eng. Sci.* **2003**, *41*, 2161–2178. [CrossRef]
10. Hayat, T.; Nawaz, M.; Obaidat, S. Axisymmetric magnetohydrodynamic flow of micropolar fluid between unsteady stretching surfaces. *Appl. Math. Mech.* **2011**, *32*, 361–374. [CrossRef]
11. Ahmad, K.; Ishak, A.; Nazar, R. Micropolar fluid flow and heat transfer over a nonlinearly stretching plate with viscous dissipation. *Math. Probl. Eng.* **2013**, *2013*, 257161. [CrossRef]
12. Reddy, G.J.; Kethireddy, B.; Umavathi, J.C.; Sheremet, M.A. Heat flow visualization for unsteady Casson fluid past a vertical slender hollow cylinder. *Therm. Sci. Eng. Prog.* **2018**, *5*, 172–181. [CrossRef]
13. Lund, L.A.; Omar, Z.; Khan, I. Mathematical analysis of magnetohydrodynamic (MHD) flow of micropolar nanofluid under buoyancy effects past a vertical shrinking surface: Dual solutions. *Heliyon* **2019**, *5*, e02432. [CrossRef]
14. Dawar, A.; Shah, Z.; Tassaddiq, A.; Islam, S.; Kumam, P. Joule heating in magnetohydrodynamic micropolar boundary layer flow past a stretching sheet with chemical reaction and microstructural slip. *Case Stud. Therm. Eng.* **2021**, *25*, 100870. [CrossRef]
15. Singh, K.; Pandey, A.K.; Kumar, M. Numerical solution of micropolar fluid flow via stretchable surface with chemical reaction and melting heat transfer using Keller-Box method. *Propuls. Power Res.* **2021**, *10*, 194–207. [CrossRef]
16. Muhammad, N.; Zaman, F.D.; Mustafa, M.T. OpenFOAM for computational combustion dynamics. *Eur. Phys. J. Spec. Top.* **2022**, 1–15. [CrossRef]
17. Muhammad, N.; Nadeem, S.; Khan, U.; Sherif ES, M.; Issakhov, A. Insight into the significance of Richardson number on two-phase flow of ethylene glycol-silver nanofluid due to Cattaneo-Christov heat flux. *Waves Random Complex Media* **2021**, 1–19. [CrossRef]
18. Fuzhang, W.; Ali, S.; Nadeem, S.; Muhammad, N.; Nofal, T.A. Numerical analysis for the effects of heat transfer in modified square duct with heated obstacle inside it. *Int. Commun. Heat Mass Transf.* **2021**, *129*, 105666. [CrossRef]
19. Crane, L.J. Flow past a stretching plate. *Z. Angew. Math. Phys. ZAMP* **1970**, *21*, 645–647. [CrossRef]
20. Dandapat, B.S.; Gupta, A.S. Flow and heat transfer in a viscoelastic fluid over a stretching sheet. *Int. J. Non-Linear Mech.* **1989**, *24*, 215–219. [CrossRef]
21. Andersson, H.I.; Hansen, O.R.; Holmedal, B. Diffusion of a chemically reactive species from a stretching sheet. *Int. J. Heat Mass Transf.* **1994**, *37*, 659–664. [CrossRef]
22. Nadeem, S.; Rehman, A.; Lee, C.; Lee, J. Boundary layer flow of second grade fluid in a cylinder with heat transfer. *Math. Probl. Eng.* **2012**, *2012*, 13. [CrossRef]
23. Majeed, A.; Zeeshan, A.; Alamri, S.Z.; Ellahi, R. Heat transfer analysis in ferromagnetic viscoelastic fluid flow over a stretching sheet with suction. *Neural Comput. Appl.* **2018**, *30*, 1947–1955. [CrossRef]
24. Pal, D.; Das, B.C. Soret-Dufour magneto-thermal radiative convective heat and mass transfer of chemically and thermally stratified micropolar fluid over a vertical stretching/shrinking surface in a porous medium. *Int. J. Comput. Methods Eng. Sci. Mech.* **2021**, *22*, 410–424. [CrossRef]
25. Muhammad, N.; Nadeem, S.; Issakhov, A. Finite volume method for mixed convection flow of Ag–ethylene glycol nanofluid flow in a cavity having thin central heater. *Phys. A Stat. Mech. Its Appl.* **2020**, *537*, 122738. [CrossRef]
26. Nadeem, S.; Ahmad, S.; Muhammad, N. Analysis of ferrite nanoparticles in liquid. *Pramana* **2020**, *94*, 1–9. [CrossRef]
27. Megahed, A.M.; Reddy, M.G.; Abbas, W. Modeling of MHD fluid flow over an unsteady stretching sheet with thermal radiation, variable fluid properties and heat flux. *Math. Comput. Simul.* **2021**, *185*, 583–593. [CrossRef]
28. Afsar Khan, A.; Batool, R.; Kousar, N. Examining the behavior of MHD micropolar fluid over curved stretching surface based on the modified Fourier law. *Sci. Iran.* **2021**, *28*, 223–230.
29. Muhammad, N.; Ullah, N. Simulation of flow on the hydroelectric power dam spillway via OpenFOAM. *Eur. Phys. J. Plus* **2021**, *136*, 1191. [CrossRef]
30. Muhammad, N. Finite volume method for simulation of flowing fluid via OpenFOAM. *Eur. Phys. J. Plus* **2021**, *136*, 1010. [CrossRef]
31. Tahir, H.; Khan, U.; Din, A.; Chu, Y.M.; Muhammad, N. Heat transfer in a ferromagnetic chemically reactive species. *J. Thermophys. Heat Transf.* **2021**, *35*, 402–410. [CrossRef]

32. Abbas, N.; Rehman, K.U.; Shatanawi, W.; Malik, M.Y. Numerical study of heat transfer in hybrid nanofluid flow over permeable nonlinear stretching curved surface with thermal slip. *Int. Commun. Heat Mass Transf.* **2022**, *135*, 106107. [CrossRef]
33. Peddieson, J., Jr. An application of the micropolar fluid model to the calculation of a turbulent shear flow. *Int. J. Eng. Sci.* **1972**, *10*, 23–32. [CrossRef]
34. Khan, W.A.; Pop, I. Boundary-layer flow of a nanofluid past a stretching sheet. *Int. J. Heat Mass Transf.* **2010**, *53*, 2477–2483. [CrossRef]
35. Wang, C.Y. Free convection on a vertical stretching surface. *ZAMM-J. Appl. Math. Mech. Z. Angew. Math. Mech.* **1989**, *69*, 418–420. [CrossRef]
36. Reddy Gorla, R.S.; Sidawi, I. Free convection on a vertical stretching surface with suction and blowing. *Appl. Sci. Res.* **1994**, *52*, 247–257. [CrossRef]